Parsimonious velocity inversion applied to the Los Angeles Basin, CA

Jack B. Muir[1,2], Robert W. Clayton[1], Victor C. Tsai[3], and Quentin Brissaud[4]

[1]Seismological Laboratory, Division of Geological and Planetary Sciences, California Institute of Technology, Pasadena, CA, USA
[2]Research School of Earth Sciences, Australian National University, Acton, ACT, Australia
[3]Department of Earth, Environmental and Planetary Sciences, Brown University, Providence, RI, USA
[4]NORSAR, Oslo, Norway

Key Points:

- We generate a new velocity model of the northeastern Los Angeles Basin using data from the Community Seismic Network
- Using a level-set framework, we parsimoniously balance the existing Community Velocity Models with new data constraints
- The new model indicates a steeper and deeper basin underneath downtown Los Angeles, significantly amplifying 4–6 s Love waves

Corresponding author: Jack B. Muir, `jmuir@caltech.edu`

Abstract

The proliferation of dense arrays promises to improve our ability to image geological structures at the scales necessary for accurate assessment of seismic hazard. However, combining the resulting local high-resolution tomography with existing regional models presents an ongoing challenge. We developed a framework based on the level-set method that provides a means to infer where local data provides meaningful constraints beyond those found in regional models - e.g. the Community Velocity Models (CVMs) of southern California. This technique defines a volume within which updates are made to a reference CVM, with the boundary of the volume being part of the inversion rather than explicitly defined. By penalizing the complexity of the boundary, a minimal update that sufficiently explains the data is achieved.

To test this framework, we use data from the Community Seismic Network, a dense permanent urban deployment. We inverted Love wave dispersion and amplification data, from the Mw 6.4 and 7.1 2019 Ridgecrest earthquakes. We invert for an update to CVM-S4.26 using the Tikhonov Ensemble Sampling scheme, a highly efficient derivative-free approximate Bayesian method. We find the data is best explained by a deepening of the Los Angeles Basin with its deepest part south of downtown Los Angeles, along with a steeper northeastern basin wall. This result offers new progress towards the parsimonious incorporation of detailed local basin models within regional reference models utilizing an objective framework and highlights the importance of accurate basin models when accounting for the amplification of surface waves in the high-rise building response band.

1 Introduction

The Los Angeles (LA) Basin is a deep sedimentary structure whose evolution can be roughly characterized by an initial subsidence and extensional phase during the establishment of the North America - Pacific plate boundary associated with the opening of the Gulf of California and the rotation of the Transverse Ranges in the Miocene. This was followed by a period of transpression (Ingersoll & Rumelhart, 1999), and the generation of a substantial network of thrust faults within the basin (Wright, 1991). In its current state, the basin contains both active strike-slip faults (e.g. the Newport-Inglewood fault, Whittier-Elsinore fault) and an imbricated stack of blind thrust faults (e.g. the Elysian Park faults, Puente hills thrust), all of which accommodate the transpressional motion of the basin. These faults contribute to local seismic hazard both by providing source surfaces for earthquakes and by controlling local path effects by shaping the basin geometry (Plesch et al., 2007). The evolutionary history of the LA basin, with ample opportunity to produce and bury organic material during extension followed by the estabilishment of stratigraphic traps during compression, allowed LA to be a leading producer of oil in the United States (US), helping to fuel a large rise in population during the mid-20^{th} century. Development took place predominantly on the soft sediments of the main LA, San Fernando, San Gabriel and San Bernadino basins. As a consequence, LA is both one of the largest and most economically important cities in the US, while also being one of the most exposed to significant earthquake hazard due to the complex fabric of active faults and ground-motion amplifying sedimentary structures associated with the geology that has allowed its preeminence.

Seismic hazard within the basin is controlled by the locations and potential for slip on the multiple local and regional faults of southern California, combined with the significant amplifying effect of the basin on ground motions. The importance of path effects, such as wavefield focusing, multipathing, and basin amplification, on LA basin ground motions has led to extensive development of seismic velocity models. The ultimate goal of these models is to produce accurate synthetic waveforms at frequency ranges relevant to infrastructure and building codes within the basin. Early efforts focused on creating rule-based models of southern California (Magistrale et al., 1996, 2000) using empirically derived velocity laws (Faust, 1951) in combination with inferred geological structure obtained by correlating surface outcrops, borehole profiles and potential methods (Wright, 1991). Since these inital efforts, regional scale models of southern California have assimilated ever greater quantities of seismic data, including seismic reflection profiles, receiver functions, and earthquake source locations and mechanisms, in an effort to better demarcate boundaries, including faults (Magistrale et al., 2000; Plesch et al., 2007), and allowed for more lateral variation of within basin velocity structures by using geostatistical methods to tie together disparate seismic data (Süss & Shaw, 2003; Shaw et al., 2015). Continued development of seismic velocity models of southern California has resulted in two widely used reference Community Velocity Models (CVMs), CVM-S4.26.M01 (Lee et al. (2014), CVM-S hereafter) and CVM-H 15.1.0 (Shaw et al. (2015), CVM-H hereafter), that have incorporated waveform based seismic tomography to further refine the models. CVM-S and CVM-H broadly agree in the positions, average velocity profile, and geometry of the major basins of southern California, however in detail they are quite different, with CVM-H containing more explicit geological information. Figure 1 shows a characteristic cross-section of the LA basin for both models, running from Catalina Island, across the Inner Borderland to Palos Verdes, then through the main LA basin, San Gabriel basin and though the transverse ranges to the high desert. This profile makes evident the considerably higher detail present in the CVM-H model due to its construction including explicit geological features (notably including an Inner Borderland basin not present in CVM-S), as well as its significant artefacts associated with changing lateral resolution, as evident in profile marks R1 and R2. In contrast, CVM-S is significantly smoother than CVM-H due to its reliance on wavefield-tomography during the final stages of construction, although several sharp resolution based artefacts are also evident. While many features of the seismic wavefield within the LA basin, such as phase arrival times and P-to-S amplitude ratios, are captured for local events at frequencies of up to 0.2 Hz (Taborda et al., 2016; Lai et al., 2020), excitations of the basin from the recent large regional Ridgecrest earthquake sequence in July 2019 have illustrated that ground motion amplification predictions from finite-difference wave propagation through the SCEC CVM-H and CVM-S models do not accurately model the observations even at the relatively low frequency 0.1-1Hz range that is relevant for tall buildings within downtown LA (Filippitzis et al., 2021), warranting continued close study of the LA basin velocity model.

Seismic tomography offers the best opportunity for full spatial coverage of the basin at high resolution, especially when dense seismic arrays are utilized. In the southern and central parts of the basin, the deployment of high-density temporary seismic arrays using 10Hz corner-frequency geophone nodes by the petroleum industry has enabled considerable exploration of the shallow structure of the basin using ambient-noise derived observables, such as Rayleigh-wave phase velocities, Rayleigh-wave amplifications, and body-wave travel times (e.g. Lin et al. (2013); Bowden et al. (2015); Castellanos et al. (2020); Jia & Clayton (2021)). However, similarly dense industry deployments have not to date taken place in the northern part of the basin, which encompasses the downtown LA region, with buildings that are highly susceptible to resonant coupling to the basin. The permanent broadband southern California Seismic Network (SCSN), while providing a long time series of excellent quality observations, has already been incorporated into the CVM reference models and does not provide the spatial resolution required for the next generation of basin models. A potential alternative data source is the Community Seismic Network (CSN, Clayton et al. (2012, 2020)), a permanent network of three-component micro-electromechanical system (MEMS) accelerometers, designed to provide real-time strong-ground-motion telemetry in the event of local earthquakes within the LA basin. The CSN instruments have been designed for inexpensive construction, utilizing off-the-shelf components, and have a maximum observable acceleration of $\pm 2g$, in order to fulfil their primary goal of strong-ground-motion monitoring. As a result, the instrument noise floor is above the amplitude of ground motions produced by smaller regional earthquakes, and is also above the ambient seismic noise level, which precludes the use of ambient-noise cross-correlation methods on CSN data as these methods rely on coherent low-level energy propagation between sensors. However, both the Mw 6.4 and Mw 7.1 2019 Ridgecrest, California earthquakes produced high quality records across the array, allowing for detailed analysis of ground amplification within the basin (Kohler et al., 2020; Filippitzis et al., 2021). The coherent surface-wave energy from these two events, recorded on the CSN, offers a unique opportunity to construct a high-resolution local tomographic model of the northeastern edge of the LA basin. In this study, we use the phase velocity and relative amplitudes of Love waves from both events, along with a 3D surface-wave tomography method based on the level-set method of Muir & Tsai (2020), to create such a model. The level-set framework extends traditional tomography by allowing for discontinuous interfaces within a velocity model, which are implicitly defined by a contour line of a latent function. For instance, Muir & Tsai (2020) used the level-set method to image the damage zone of the San Andreas Fault at Carrizo plains using a an implicit three-layer model, while Tso et al. (2021) presented several applications of the level-set method for developing interpretable block models of electrical resistivity. The ability to handle implicitly defined discontinuities significantly extends traditional tomography, which usually require restrictive and unphysical regularization schemes to be well-posed. We use the level-set method to define a basin volume within which we update a local model — this method allows us to only alter the reference CVM model where we have sufficient data constraints to warrant an update. Integration of local models within the SCEC CVM ecosystem will become an important part of hazard modelling within Southern California as high-density arrays allow access to the fine scale detail of path effects. The framework presented in this study represents a parsimonious way to achieve this integration.

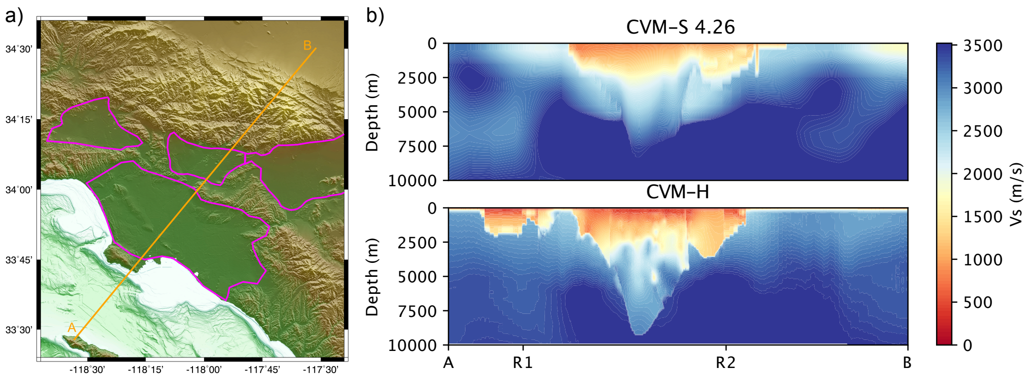

Figure 1. a) Shaded elevation model of southern California showing the outline of the major basins (defined by slope-break analysis) in purple and the transect A-B used for profiles shown in orange. b) Characteristic profiles through the Los Angeles basin for the CVM-S and CVM-H models. Abrupt lateral changes in resolution at positions R1 and R2 are seen in the CVM-H model.

2 Data Collection

2.1 Preprocessing

The data for this study were obtained from the HN accelerometer channels of the Los Angeles Unified School District (LAUSD) subarray of the Community Seismic Network (CSN, Clayton et al. (2012, 2020)), consisting of 200s time series after the Mw 6.4 and Mw 7.1 Ridgecrest earthquakes' origin times and recorded at 50 samples/sec. The network is deployed within school buildings in the City of Los Angeles, and at the time

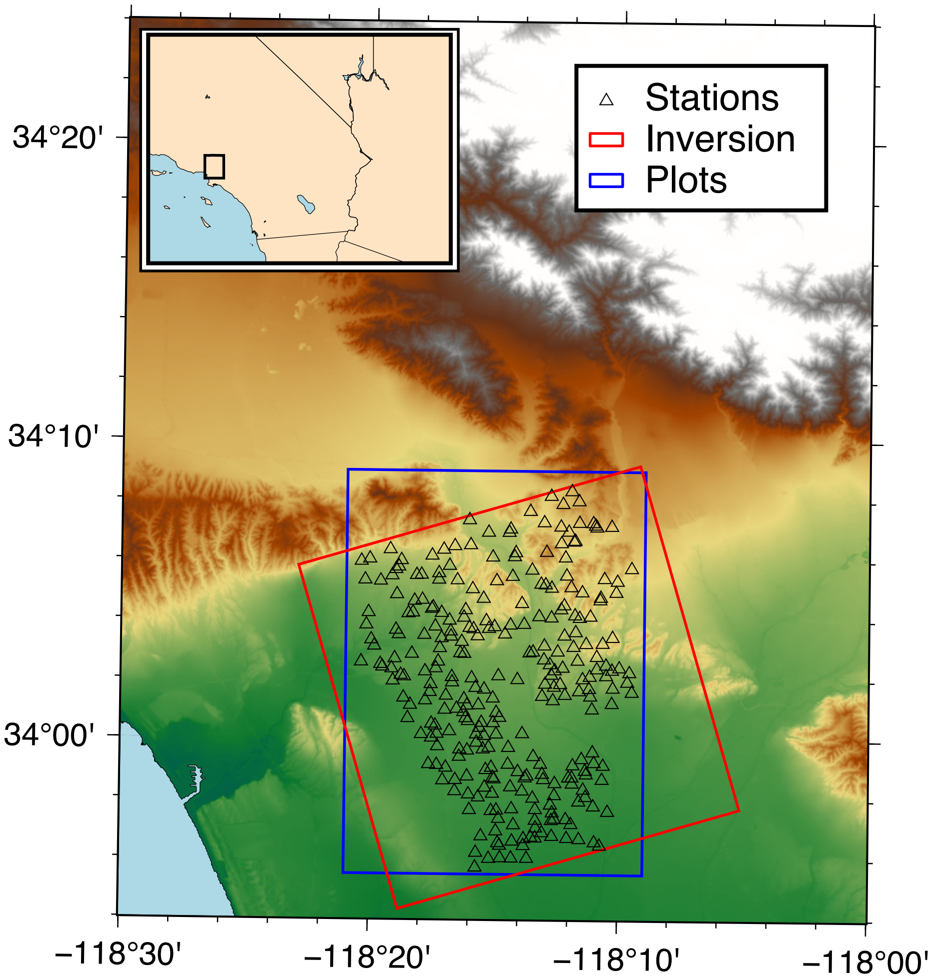

Figure 2. Map of the study region, showing the locations of the CSN stations as empty triangles, the boundary of the square inversion region in red, and the boundary of the analysis plots in blue.

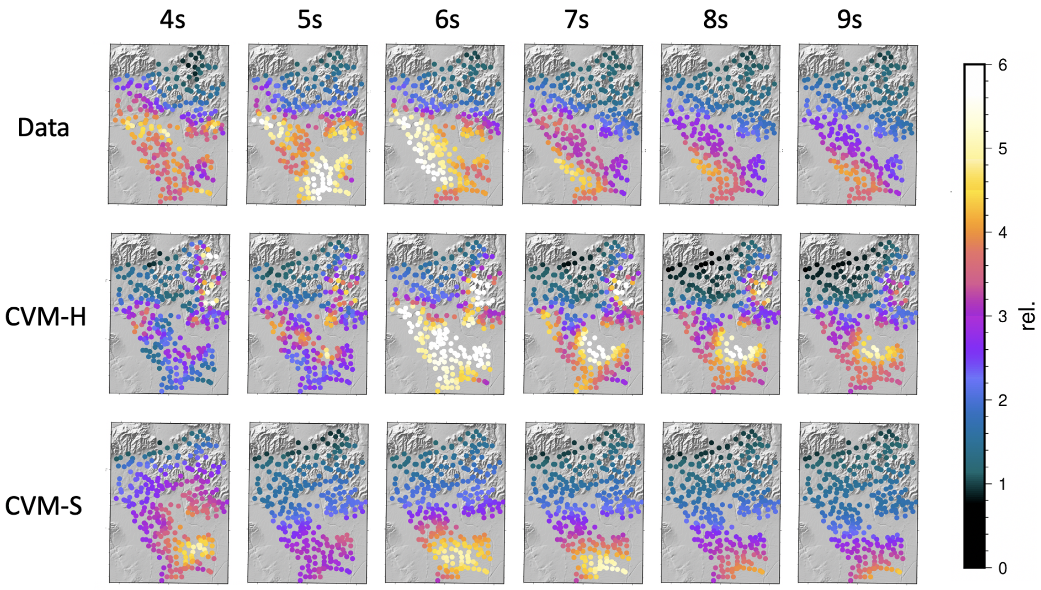

Figure 3. Relative amplification of the maximum amplitude of 3 component pseudo-spectral accelerations (PSA) in the range of 4–9 s from the Mw 7.1 July 5 2019 Ridgecrest Earthquake as recorded on the Community Seismic Network (CSN), and as simulated using the Graves and Pitarka rupture generator (Pitarka et al., 2019) and a 3D finite-difference waveform solver for both the CVM-H and CVM-S models.

of the Ridgecrest earthquakes consisted of 300 stations spaced approximately 0.5 km apart. We used the components of the CSN located within the northeast LA basin, which is the densest part of the array — the study area, including the locations of the stations, is shown in Figure 2. Various display of the Ridgecrest earthquake data are shown in Filippitzis et al. (2021), along with a comparison of the data and predicted ground motions by several methods. For our study, data were first detrended, rotated into the ZRT frame, decimated to 5 Hz and then detrended once more. Pseudo-spectral accelerations (PSA) were then calculated for both the real data and synthetic 3D finite-difference simulations following the Graves and Pitarka method (Graves & Pitarka, 2010; Pitarka et al., 2019) for both the CVM-H and CVM-S models by convolving the records with a 5% damped harmonic oscillator, with the results for 4–9 s period shown in Figure 3. A record section of the high-frequency strong-ground-motion-accelerometer transverse (HNT) channel showing strong SH polarized phases corresponding to the fundamental Love mode is shown in Figure 4.

2.2 Love Group Arrival Time and Amplitude Picks

To make group arrival picks, raw waveforms were first narrow-band filtered at period P using a zero-phase Butterworth bandpass filter with corners at $1/P \pm 1/(\sqrt{20}P)$ and then cosine tapered over the first 20s of the time series to suppress edge effects. The maximum of the T component envelopes at a central period $P = 12.5$s were set as the first preliminary group arrival pick. The 12.5s filtered waveform envelopes were then again cosine-tapered with a $6P$ taper window with $1P$ edges about this preliminary pick. We then fit a Gaussian function to the waveform envelope, with the center of the Gaussian being used as the finalized group arrival pick at 12.5s and the amplitude of the Gaussian being recorded as the Love wave amplitude. Starting with the parameters of the 12.5s Gaussian as initial values, we then proceeded to work down in 0.25s increments on the

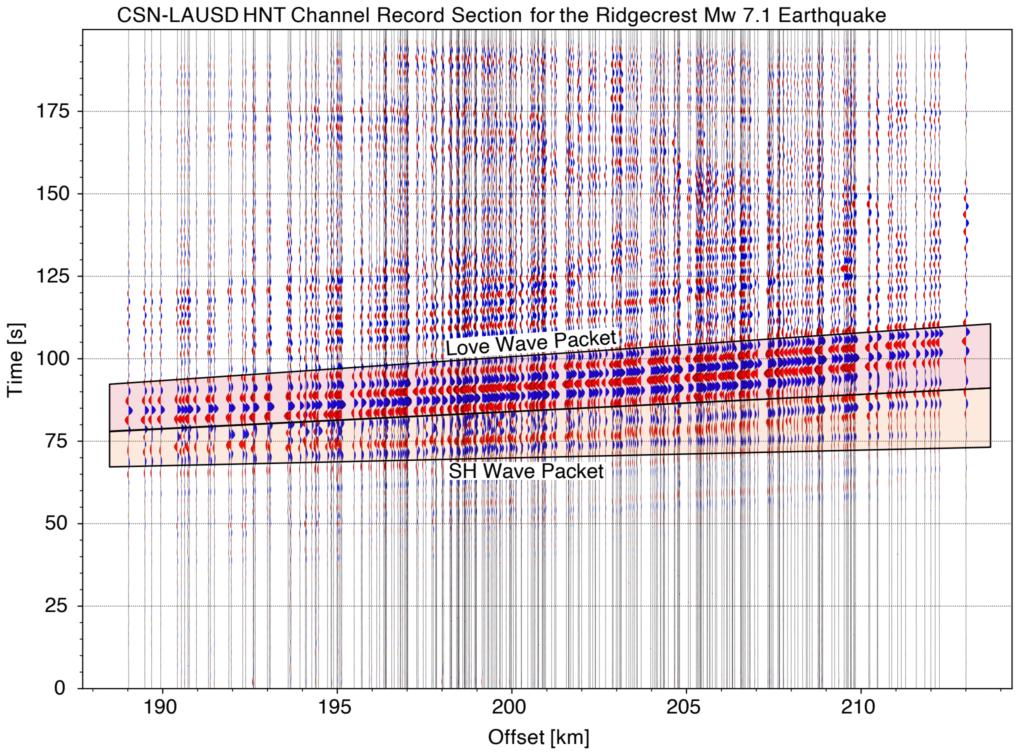

Figure 4. Record Section of the Mw 7.1 Ridgecrest earthquake as recorded on the HNT channel of the CSN-LAUSD array, zero-phase bandpass filtered between 4–10s. Two main phases are clearly identifiable, with the first arriving phase exhibiting little delay due to the basin at longer offsets, which we infer to be the primary SH arrival, which is shaded orange. A second, stronger phase, which is delayed by the basin at longer offsets, we infer to be the fundamental Love mode and is shaded red.

narrowband filtered waveform envelopes, to a minimum period of 2s. We tapered with the $6P$ width cosine around the Gaussian center of the previous period. We then fit a new Gaussian to the shorter-period waveform, initialized using the previous period's Gaussian fit. This method tracks the Love-wave group arrival from long periods, where it is clearly identifiable as the strongest feature, to shorter periods where other features are present. A characteristic example of the group picks is shown in Figure 5.

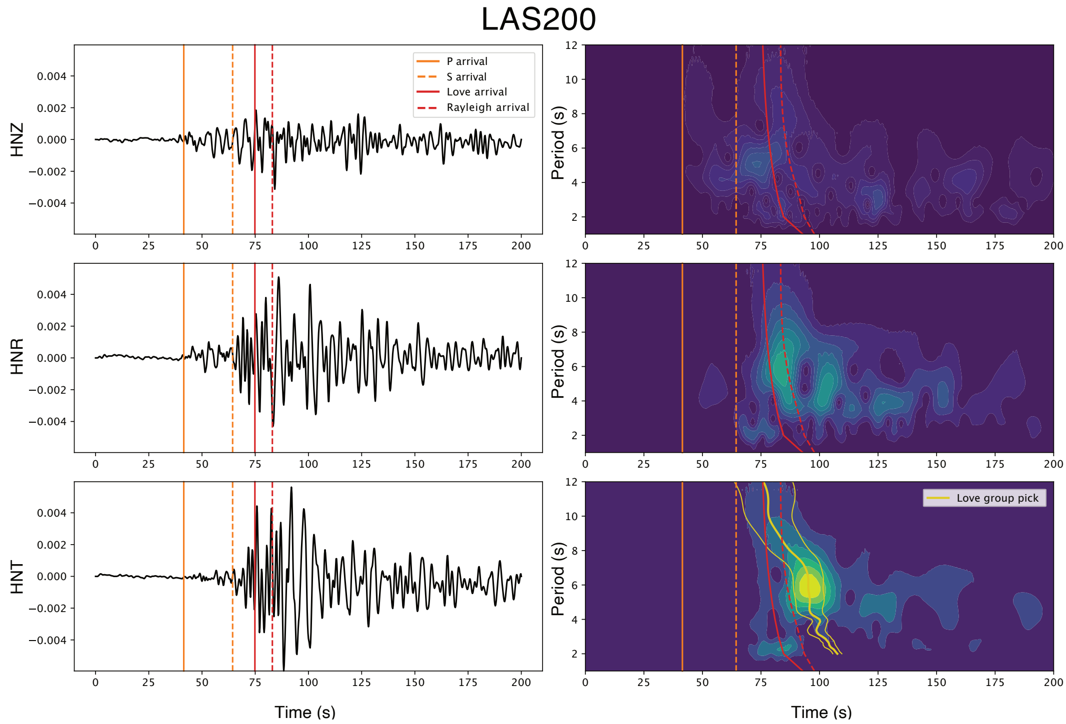

Figure 5. HN waveforms and corresponding continuous-wavelet transform spectrograms for the LAUSD CSN station LAS200 from the July 5 2019 Ridgecrest Mw 7.1 earthquake. The solid and dashed orange lines show the theoretical arrival times of the P and S waves through the laterally averaged CVM-H model from the hypocentral location to LAS200, and the solid and dashed red lines show the theoretical group arrivals for Love and Rayleigh waves, respectively. All theoretical travel times are offset from the event origin time by 10s, which is the approximate peak of the USGS moment rate function. The lemon yellow lines show the center and $\pm 1\sigma$ width of the fitted Gaussian functions to the envelope of the tangential component. The center of these Gaussian functions act as group delay picks for defining the cross-correlation window used for two-station phase delay measurements shown in Figure 6.

We took the logarithms of the fitted Gaussian amplitudes and normalized them relative to the mean log at each period to create the amplitude data set. The relatively narrow aperture of the CSN array compared to the distance to the source meant that the geometry was not favorable for traditional tomographic methods. We therefore employed eikonal tomography (Lin et al., 2009, 2014) to calculate surface-wave dispersion curves, which has the additional advantage of naturally handling the curving wavefronts recorded on the CSN, caused by refraction across the basin boundary. While recent studies (Qiu et al., 2019) have attempted to utilize group arrival times for eikonal tomography of group velocity, there is significant noise associated with the group arrival peak. Furthermore, there are strict conditions on the approximations necessary for using eikonal tomography on group delay times which may not be met when the surface-wave arrival experiences refraction across a basin boundary. As such, we did not attempt to utilize group velocity c_g in this study, but rather used the group times as a guide for two-station cross-correlation phase delay times as discussed below.

2.3 Eikonal Tomography from Two-Station Cross-Correlation Phase-Delay Times

We employ eikonal tomography (Lin et al., 2009) to obtain phase velocity estimates within the densely spaced CSN array. Eikonal tomography obtains phase velocity c directly from the gradient of the phase delay field: $|\nabla\tau| \approx 1/c$. Eikonal tomography has two principle requirements. Firstly, there must be a clearly identifiable phase delay field τ (i.e. there is no significant multipathing), a requirement which is met for Love waves in the period range of this study. Secondly, eikonal tomography is derived from an approximation of the transport equation $1/c^2 = |\nabla\tau|^2 - \nabla^2 A/A\omega^2$, where ignoring the amplitude correction is typically taken to be valid for velocity models that are sufficiently laterally smooth that the amplitude Laplacian is small. Waves propagating from the Ridgecrest earthquake sequence strike the northeastern edge of the Los Angeles Basin nearly perpendicularly, so any effect of the basin edge on the Laplacian is limited in extent within the LAUSD-CSN array. It is possible to utilize the full transport equation for determining phase velocity, which is called Helmholtz tomography (Lin & Ritzwoller, 2011), however comparisons between Helmholtz tomography and eikonal tomography show agreement across the basin transition where we would expect the amplitude correction to be strongest, implying that eikonal tomography is sufficient to capture the correct phase velocity in the center of the array. Spurious values of the Helmholtz tomography solutions occur on the edges of the array due to the difficulty of obtaining accurate values of the amplitude Laplacian. Consequently, we limit our data analysis to the phase velocities derived from the eikonal equation as its assumptions appear to be satisfactorily realized and the Helmholtz tomography corrections are not sufficiently robust given our data.

In order to obtain the phase delay field τ at period P (relative to the northernmost station of the array), we first narroband filter wavepackes using central period P and cosine tapered with a flat pass window of width $4P$ and edges of P centered at the group arrival time. We then calculate the cross-correlation time delay $\Delta\tau_{ij}$ between each pair of stations i and j within a circle of radius $r_{ij} < \max(c_g P, c_{min} P)$ with a cutoff velocity $c_{min} = 0.5$km/s. The distance limit reduces the impact of potential cycle skipping on the phase delay observations, while the narrower taper width compared to the group picks also helps to stabilize the cross-correlation calculations. This process is illustrated in Figure 6 a) and b). The relative delays $\Delta\tau_{ij}$ form a graph with stations acting as nodes and the delays acting as edge weights. Similarly, the distances between stations Δd_{ij} also form a graph. Appealing to Fermat's principle of least travel time, we extract the minimum spanning tree (MST) of the station distance graph, and then use the geometry of the MST to find the minimum travel time surface. The MST is a unique sub-graph that connects all nodes (stations) with minimum edge weights (distances), with a schematic of this subgraph shown in Figure 6 c). Summing phase delays $\Delta\tau_{ij}$ along MST edges from the northernmost station gives a minimum relative travel time surface that is concordant with the observed phase delay data, as shown in Figure 6 d). We also tested MSTs extracted from the graph of normalized cross-correlation values, as well as the phase delays themselves, but found that distance weighting gave the best performance. We then smooth the travel-time surface at each period by first fitting a high-tension cubic spline to the data, removing all outlying data points for which the fit residual at that point were greater than one standard deviation of all collected residuals, and then refitting the spline to the remaining data. This smoothed surface τ is then used to calculate phase velocity c at period p using the eikonal equation $|\nabla\tau| = 1/c$.

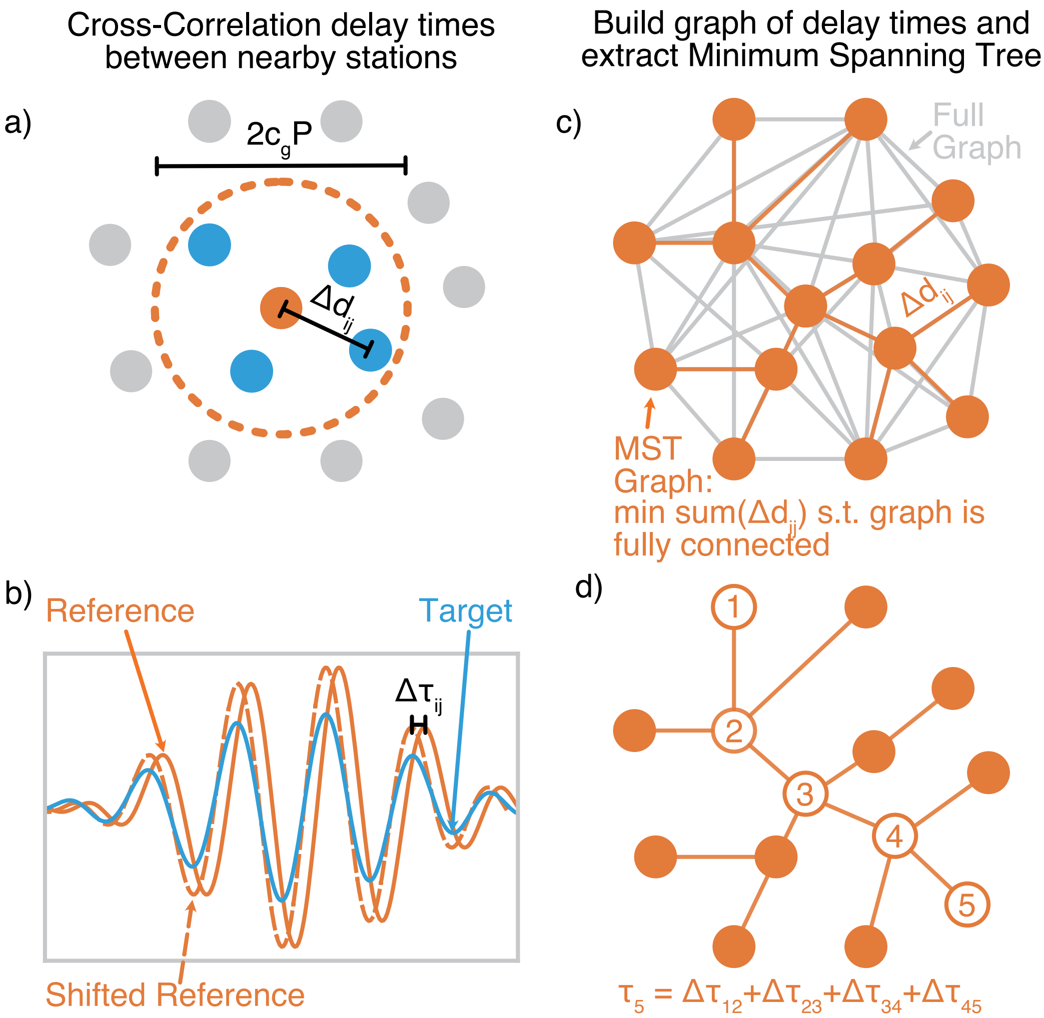

Figure 6. Outline of steps used to construct the phase delay field τ from narrowband filtered records. In the first two steps, the phase delays between all nearby stations are computed. In a), we draw a circle of radius $r_{ij} < \max(c_g P, 0.5P)$ and compute the phase delay for maximum cross-correlation, $\Delta\tau_{ij}$, as shown in b). Only nearby stations are used to suppress cycle skipping. In the second phase, we extract the minimum spanning tree (MST) from the graph of collected phase delay times, as shown in c). The MST is a sub-graph which minimizes the total edge lengths (i.e. Δd_{ij}) such that the graph is still fully connected. Finally, in d) we unroll the MST from the northernmost station, summing $\delta\tau_{ij}$ along the edges to get the τ, a minimum-relative-phase-delay surface concordant with the recorded relative phase delays between individual station pairs.

2.4 Estimating Measurement Uncertainty

The only available earthquakes that have produced sufficiently strong ground motions to record at least one octave of frequencies of Love waves are the Mw6.4 and Mw7.1 Ridgecrest events. Two events are insufficient to obtain useful statistical estimates of measurement uncertainty at each individual station. However, given that the surface-wave measurements have a finite area of sensitivity that overlaps substantially between neighbouring stations, we may bin error statistics over subarrays of radius $\lambda/4$ to obtain an estimate of the measurement uncertainty, where λ is the wavelength at the period of measurement. At station i, we calculate the mean of the relative log amplitude $\tilde{a}^i = (a^i_{6.4} + a^i_{7.1})/2$ and phase velocity $\tilde{c}^i = (c^i_{6.4} + c^i_{7.1})/2$ where $a_{6.4}$ and $c_{6.4}$ are the amplitude and phase velocities for the Mw 6.4 earthquake, respectively, and likewise $a_{7.1}$ and $c_{7.1}$ are the amplitude and phase velocity for the Mw 7.1 earthquake. We then estimate the standard error in the mean by averaging over errors at nearby stations:

$$\sigma_a^i = \sqrt{\sum_{j\in d_{ij}\leq\lambda/4}\left(a^j_{6.4} - \tilde{a}^j\right)^2 + \left(a^j_{7.1} - \tilde{a}^j\right)^2}/\sqrt{2} \quad (1)$$

$$\sigma_c^i = \sqrt{\sum_{j\in d_{ij}\leq\lambda/4}\left(c^j_{6.4} - \tilde{c}^j\right)^2 + \left(c^j_{7.1} - \tilde{c}^j\right)^2}/\sqrt{2} \quad (2)$$

where d_{ij} is the distance between stations i and j. The error correlation matrix P_{ij} is estimated using a squared-exponential kernel with characteristic lengthscale equal to one quarter of the average wavelength between the two stations, with the addition of a diagonal term to account for uncorrelated error

$$P_{ij} = \delta_{ij} + \exp(-8d_{ij}^2/(\lambda_i + \lambda_j)^2), \quad (3)$$

where δ_{ij} is the Kronecker delta. For each period the error covariance matrices are therefore given by $\Gamma_c = \sigma_c P \sigma_c^T$ and $\Gamma_a = \sigma_a P \sigma_a^T$ where σ_c is the collected vector of individual station phase-velocity error measurements across all periods, and σ_a is likewise the vector of amplitude error measurements. Future work on error modelling could account for a variable scaling between the diagonal and non-diagonal terms in P, and model the correlations between measurements at neighboring periods; however for reasons of computational expediency we do not develop these analyses here.

3 Inversion Methodology

3.1 Model Parameterization

Having obtained measurements $\tilde{c}$ and $\tilde{a}$ and associated error matrices Γ_c and Γ_a for phase velocity and log-relative amplification within the CSN, we are now in a position to model them and invert for a local basin update. We seek to obtain a parsimonious local update that balances the constraints of new, densely recorded data, with the already well developed models presented in the SCEC CVMs. Ideally, we would perform a fully Bayesian inversion taking a CVM as a prior model; however as robust model uncertainties for the CVMs are not available, this approach would be highly dependent on subjective estimates for setting the prior, and would furthermore be extremely computationally expensive for the nonlinear forward models required to predict our recorded data. Instead, we recognize that the sensitivity of our data is highly contained within the basin itself, given the characteristic phase velocities c and periods p of our study and the heuristic sensitivity depth of $cp/4$ for Love waves in a power-law basin-style velocity profile, given by Haney & Tsai (2020). Taking advantage of this restricted sensitivity, we utilize the level-set-tomography framework of Muir & Tsai (2020) to explicitly define a volume within which we perform our model updates as part of the model parameterization, and appropriately regularize the boundary of this volume to achieve the desired parsimony between the *a priori* CVM model and constraints from our newly observed data.

In this study, our model parameterization consists of two parts — a boundary to the inversion domain, and the velocity perturbations within that domain. Both components of the model are given by Gaussian Processes (GP) with a Whittle-Matérn kernel — briefly, this GP model supposes that the outputs are jointly distributed like a multivariate normal distribution with a pairwise covariance between model points with spatial locations x and x' given by

$$C(x, x') = \sigma^2 \frac{2^{1-\beta}}{\Gamma(\beta)} \left(\frac{||x - x'||}{l} \right)^{\nu} K_\beta \left(\frac{||x - x'||}{l} \right), \tag{4}$$

where Γ is here the gamma (or extended factorial) function and K_β is the modified Bessel function of the second kind. A comprehensive treatment of classical GP models may be found in (Rasmussen & Williams, 2006). The statistical properties of the GP are controlled by its hyperparameters, which for the Whittle-Matérn kernel are l, the characteristic length scale, σ the characteristic scale of perturbations, and β the regularity parameter. Individual realizations of the GP are $\beta - \frac{1}{2}$ times continuously differentiable. In practice β is very hard to infer in most inverse problems and so it is set to $\beta = 3\frac{1}{2}$ for the remainder of this study, a choice which generates sufficiently smooth models to ensure that Love-wave eigenvalues are correctly calculated, and which does not introduce artificial roughness into the posterior distribution.

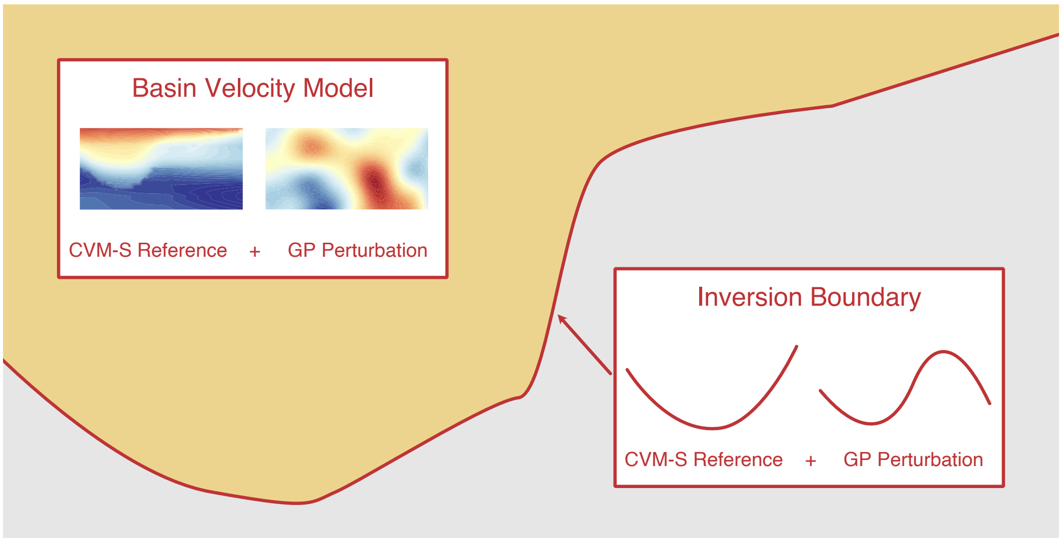

Figure 7. Schematic of the model definition, showing the construction of the velocity model update and the boundary of the inversion, both constructed from a CVM-S reference perturbed by a Gaussian Process. The background model, schematically shown in grey, is given by the unaltered CVM-S model.

GP models with variable hyperparameters offer great flexibility, however they are expensive to compute in the spatial domain as they require repeated inversion of the covariance matrix C — an operation of complexity $O(n^3)$ for n model evaluation points. To accelerate the GP computations, we approximate the model by defining it on a regular grid with n_{cell} grid nodes in each dimension, which allows us to specify the model by means of its Fourier coefficients ξ_v and ξ_b for the velocity and inversion boundary components respectively (Lindgren et al., 2011; Chen et al., 2019). Efficient sampling of the GP can then be performed by an inverse Real Fast Fourier Transform (complexity of order $O(3m^3 \log(m))$ where $m = n_{cells}/2 + 1 \ll n$), followed by interpolation by cubic splines to the locations required for computing the forward model for phase velocity and amplitude underneath each station. We use the same lengthscale parameter l for both the velocity update and the inversion boundary; the inversion domain is $22 \times 22 \times 12$ km in size, which must be rescaled to a unit cube for the inverse Fourier transform. The inversion area was determined by finding the smallest square that encompassed the stations, and is shown in in Figure 2. We use 16 cells in each dimension, and a rescaled $\tilde{l}$ parameter on the unit cube domain, which induces an effective lengthscale of $l_{xy} \sim 22\tilde{l}$ in the horizontal direction and $l_z \sim 12\tilde{l}$ in the vertical direction – equivalent to assuming vertical heterogeneity approximately twice as sharp as lateral heterogeneity. We denote the evaluation (via inverse FFT) of the velocity GP model given velocity Fourier coefficients ξ_v, lengthscale $\tilde{l}$ and velocity characteristic perturbation amplitude σ_v at a location (x, y, z) by $GPV_{\xi_v,\tilde{l},\sigma_v}(x, y, z)$, and the evaluation of the inversion boundary given boundary Fourier coefficients ξ_b, lengthscale $\tilde{l}$ and boundary characteristic perturbation amplitude σ_b at a location (x, y) by $GPB_{\xi_b,\tilde{l},\sigma_b}(x, y)$. For both GP models, a Whittle-Matérn kernel is assumed, and we use the CVM-S velocity model and basin profile to set mean to ensure initialization near a physical solution. CVM-S was chosen over CVM-H as the mean due to its smoothness, which lends itself to more concordant velocity models across the inversion boundary, and also because it better fits waveforms within the basin (Lai et al., 2019).

The V_s model is therefore given by

$$V_s(x,y,z) = \begin{cases} V_{\text{CVM-S}}(x,y,z) + GPV_{\xi_v,\tilde{l},\sigma_v}(x,y,z) & z < z_{\text{CVM-S}}(x,y) + GPB_{\xi_b,\tilde{l},\sigma_b}(x,y) \\ V_{\text{CVM-S}}(x,y,z) & z \geq z_{\text{CVM-S}}(x,y) + GPB_{\xi_b,\tilde{l},\sigma_b}(x,y), \end{cases} \tag{5}$$

where $V_{\text{CVM-S}}$ and $z_{\text{CVM-S}}$ are the S velocity model and basin edge extracted from CVM-S. A graphical schematic of the definition of the discretized model is shown in Figure 7. Density and V_p are then calculated from the V_s model using the empirical relationships of Brocher (2005), which are suitable for basins within southern California.

3.2 Extracting Reference Basin Depth Profiles from CVM-S

The SCEC CVM-S model is defined by a gridded voxel parametrization of V_P, V_S and ρ i.e. it does not contain explicit definitions of basin boundaries. To obtain reference boundaries for the CVM-S model, we utilized the following procedure. At each depth slice, we computed the mean and standard deviation of V_S. We then flagged each voxel for which V_S was slower than one standard deviation below the mean of that depth slice as a potential basin candidate. For each 1D depth profile, we then worked from the second (z=500m) depth slice downwards, flagging a voxel to be within a basin only if all voxels above it were also flagged — working from the second depth slice avoids the connection of individual basins due to artificial connectivity in the absence of the geotechnical layer. This process encodes an assumption that basins are strictly convex, which is not true in general but is a useful approximation to begin the inversion process. Using the *scipy* module *ndimage* (SciPy 1.0 Contributors et al., 2020), we then performed image segmentation using the *label* function, which generated 61 individual basins in southern California, of which the most prominent correspond to the Ventura Basin, combined Los Angeles and San Gabriel basins, San Fernando Basin, and the Salton Trough. This workflow is presented in Figure 8. The boundaries of the Los Angeles / San Gabriel basin candidate were then utilized as the reference basin bottom surface for the inversion step.

3.3 Forward Modelling

In order to predict the data from the final rasterized velocity model given by our model parametrization, we employ the lumped-mass finite element method for surface-wave eigenvalue calculation first proposed by Lysmer (1970), and implemented for Love waves by Haney & Tsai (2020). The rasterized model is interpolated onto a set of finite elements of exponentially increasing thicknesses h given by $h_n = \min(c) * \exp(N/(na))/n$

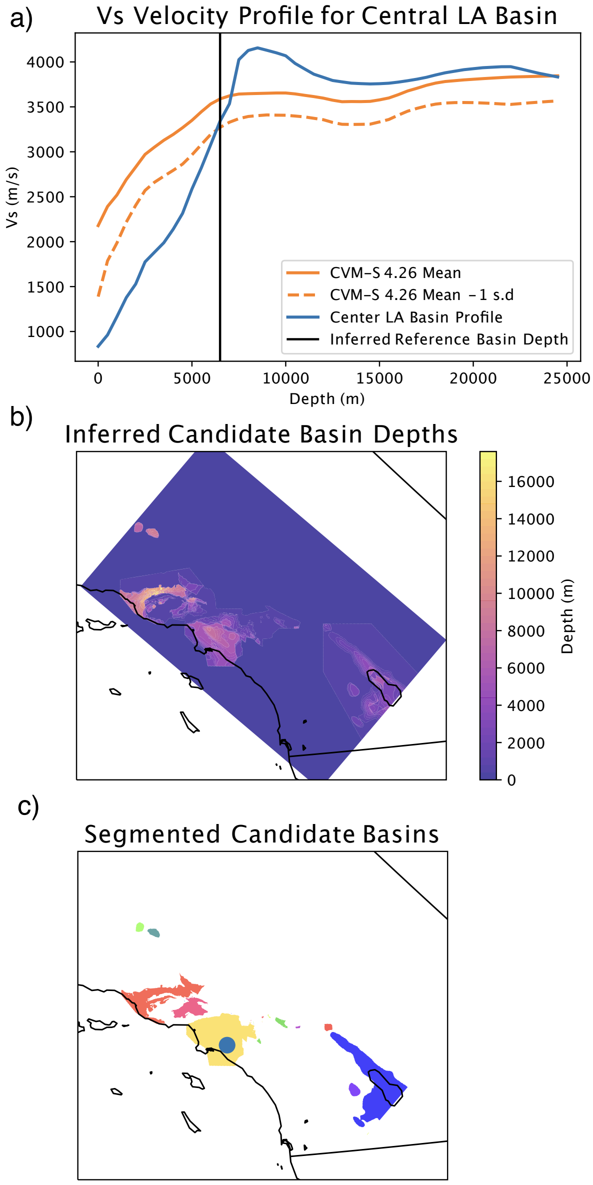

Figure 8. Outline of steps used to extract a reference basin surface from the CVM-S. a) for each vertical profile in CVM-S, we determine where (if anywhere) the V_S profile first becomes faster than one standard deviation below the mean CVM-S at that depth. All depths above this level are set to be a potential candidate basin at the location of the profile. In b), we show the extracted candidate basin depths across southern California. In c), we strip off the top 500m (which is highly connected) and then use the SciPy *ndimage label* function to segment the remaining data volume. The three major basin families of southern California are clearly seen in pink (Ventura / San Fernando), yellow (Los Angeles / San Gabriel / San Bernadino) and blue (Salton Trough).

where $N = 50$ is the number of layers in the model, $\min(c)$ is the minimum phase velocity in a reference model, and $a = 0.25$ is a constant used to control the exponential scaling. This exponential scaling heuristically balances the need for finer resolution near the top of the model when calculating shorter period Love waves in a way that is near optimal due to the approximate exponential shape of Love eigenfunctions (Tsai & Atiganyanun, 2014; Haney & Tsai, 2015, 2017, 2020). These layers are stacked on top of 4 layers of thickness $h = 10$ km simulating an infinite half-space to avoid contamination with the locked lower boundary condition. We then set up the finite element stiffness and mass matrices as given by Haney & Tsai (2020), and solve for the maximum slowness eigenfunction u that corresponds to the fundamental Love mode, as well as the phase velocity $c = \sqrt{\nu}\omega$, with ν being the eigenvalue associated with u for angular frequency ω, and group velocity c_g which is a function of c, u and the finite-element mass and stiffness matrices. The relative amplification of Love waves directly observed between two locations can then be calculated by

$$\frac{a_1}{a_2} = \left(\frac{c_{g_1} I_1}{c_{g_2} I_2}\right)^{-1/2}, \tag{6}$$

with $I = \int_0^\infty \rho(z) u(z)^2 dz$ (Bowden & Tsai, 2017; Bowden et al., 2017). Transmission coefficients obtained using a 1D mode-conversion theory (Datta, 2018; Brissaud et al., 2020) are plotted in Figure 9, and suggest that any potential modelling error from neglecting mode-coupling is small. As we use a derivative-free inversion method, these quantities are sufficient to solve for the optimal model.

3.4 Inverse Solver

We use an extension of the Ensemble Kalman Sampler (EKS, Garbuno-Inigo et al. (2020)) to perform the inversion. This method uses an interacting ensemble of particles that follow Langevin diffusion dynamics to infer a Gaussian approximation to the posterior of the inverse problem. The EKS is derivative-free and embarrassingly parallel in the forward model, which enable rapid user iteration between different datasets and forward modelling methods, as well as easy deployment on heterogenous computing networks. The EKS as outlined in Garbuno-Inigo et al. (2020) assumes that all model parameters have a Gaussian prior. This restricts the model to have fixed hyperparameters (e.g. $\tilde{l}$, σ_v, σ_b, as required to set the statistical behaviour of the model parameterization described in Section 3.1), which introduces a significant potential for practitioner bias as we do not have a good basis for estimating these *a priori*. Consequently, we have further developed the EKS to handle hierarchical models with variable hyperparameters. The original EKS and our extension to it are discussed in detail in Appendix Appendix A. The priors for the velocity hyperparameters are given by $1/\tilde{l} \sim Normal(0, 0.6)$ and $\sigma_v \sim Normal(0, 0.1)$ in scaled inverse km and km/s respectively. Experimentation has shown that the characteristic boundary perturbation amplitude σ_b is not sufficiently identifiable from our data, so we set it to a reasonable value of 0.5 km that is small enough to avoid large, unrealistic changes in the basin geometry whilst allowing a sufficient fit to the data. Using these hyperpriors, we run hierarchical EKS sampling using an initial step length $\Delta t_0 = 50$, and an ensemble size of 32. We double both the step length and the ensemble size every 50 iterations up to iteration 250, and further double the step length only at iteration 300, to finish with 400 iterations. The purpose behind this doubling scheme is to rapidly approach the *maximum a posteriori* (MAP) point using rough gradients from a small number of ensemble members, and then perform more accurate sampling of the posterior using more ensemble members (Garbuno-Inigo et al., 2020). The step length doubling counteracts the tendency of the gradient amplitude to be small near the MAP point. Convergence diagnostics for the inversion run are shown in Figure 10. The final inversion reduced the weighted Gaussian misfit function from 8.79 (for the CVM-S model) to 5.33, a variance reduction of 22%, which is a notable improvement from the already highly optimized reference model.

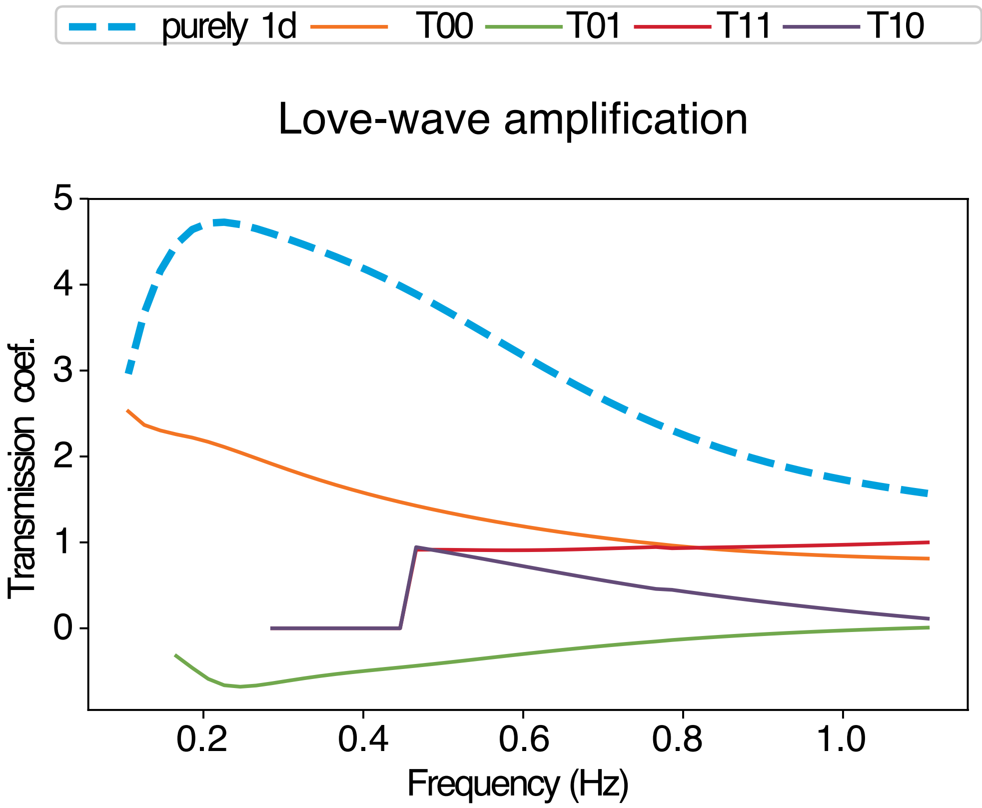

Figure 9. Transmission coefficients for a Love wave entering the Los Angeles basin obtained using a 1D mode-coupling theory (Datta, 2018; Brissaud et al., 2020). This represents a worst-case mode-conversion scenario, with the true basin exhibiting a smoother horizontal gradient and hence less conversion. Even in this case, the conversion of energy from the fundamental mode to first overtone T_{01}/T_{00} is relatively small, suggesting that our use of classical Love-amplification theory is appropriate.

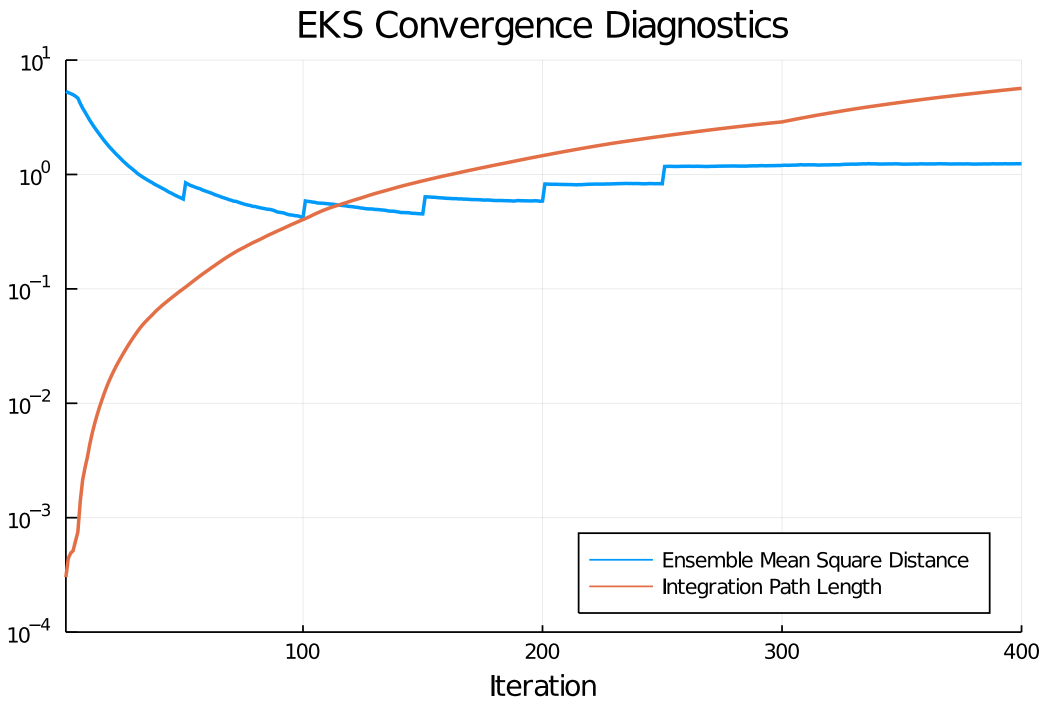

Figure 10. Convergence diagnostics of the Ensemble Kalman Sampler (EKS) showing the Ensemble Mean Square Distance converging to a constant approximation of the posterior, and the integration path length increasing steadily (heuristics from Garbuno-Inigo et al. (2020) suggest a path length of 2 is sufficient to approximate the posterior).

4 Results and Implications for the Los Angeles Basin

The results of the inversion are shown in Figures 11, 12 and 13. In Figure 11 we plot the mean depth to the inferred basin bottom and the inferred change in the depth of the Los Angeles basin at each station. The change in basin depth is defined by the difference between the reference basin depth extracted from the CVM-S in Section 3.2, and the depth to the same velocity contour in the final model. Figure 12 shows the details of the inversion along the profile A–A'. Figure 13 shows the approximate posterior distribution of the hyperparameters in the inversion. In Figure 12, we also show the reference CVM-S model used to initalize the inversion, the mean of the EKS ensemble, the difference between these two, and the standard deviation of the ensemble. The standard deviation gives a sense of the relative uncertainty of the final inversion; as discussed in Garbuno-Inigo et al. (2020), in the low-particle limit EKS sampling cannot fully capture the range of uncertainty in the true inversion posterior, and so the plotted standard deviations are best assessed in a qualitative fashion. The EKS ensemble indicates that the highest uncertainties are along the boundary of the model. Within the inverted area of the final model, the uncertainties are highest in the deep central basin where the 4-10s Love wave period range offers less sensitivity, and near the northeastern edge of the model where the phase velocities are high, resulting in small travel time gradients and hence higher uncertainties when employing eikonal tomography.

There are two principle features that are apparent from the results of the inversion. The first and most significant finding is that the data supports a deeper Los Angeles basin along its northeastern edge, with an especially large jump in basin depth in the area immediately abutting the Upper Elysian Park fault as defined in the USGS Quaternary fault map (USGS, 2020). The increase in basin depth reaches its maximum just south of downtown LA, as is seen in the south part of Figure 11 b) which shows the change in basin depth. The Upper Elysian Park fault is shown by a thick dashed cyan line in the center-right of the panels of Figure 11, and demarcates a steep gradient in the edge of the basin which has been accentuated as a result of the inversion. In Figure 12, this tall jump in the depth of the basin edge occurs in the center of the profile A-A', with Figure 12 c) showing that the deep parts of the basin to the SSW of the fault are significantly slower in our final model, with the edge of the basin being significantly steeper in our model in a) than the reference model in b). This steepening is spatially coincident with the observations of high amplification further north in the data than in the reference models, seen in Figure 3, particularly in 5–7 s band. Extracting the average basin edge gradient from 11.25–13.25 km along profile A–A' in Figure 12 gives a dip angle of 72–73°. The SCEC CVMs have evolved from the original models of Magistrale et al. (1996, 2000), which for the Los Angeles basin were based on an empirically determined velocity law for compacted sediments (Faust, 1951), with the spatial distribution of velocities controlled by contacts between two gross scale units (the Repettian and Mohnian), and the inferred basement depth, as reported in Wright (1991). There is a notable gap in the locations of control wells used by Wright (1991), which in turn initialized the SCEC CVMs (either as a starting model for full-waveform inversion used in CVM-S (Lee et al., 2014) or included as a constraint in CVM-H (Tape et al., 2009; Shaw et al., 2015)), across the steep northeastern boundary of the basin that is now covered by the CSN. Given the position of the basin sidewall is situated between the imbricated blind-thrust faults of the Elysian Park system (Plesch et al., 2007), the high apparent dip angle imaged by surface-wave measurements gives further support to an over-thrusted basin in this region (as is included in the CVM-H model, albiet further to the northeast than is suggested by our results). Further cross-sections through the model are shown in Figure 14, and show that this steep basin sidewall continues along the northwest-southeast axis of the northern LA basin wall.

The second notable finding is that the depth of the low velocity zone in the hilly terrain north of the Los Angeles basin is substantially shallower than in the reference model, which can be seen both along the northern edge of Figure 11, and in the faster velocities around end A' of the transect in Figure 12 c). This shallowing of the basin relative to the CVM-S model is somewhat unsurprising given the high Love wave speeds recorded in the northeast of the array from eikonal tomography, and the relatively lower amplification when compared to the slow, deep sediments in the central basin. Indeed, the northeastern components of the CSN operate within the surface expression of the lower Puente and Topanga units of the LA basin stratigraphic column, which were assembled early within the LA basin sequence and support a shallow sequence of basin rocks towards to the right of profile A-A' (Yerkes et al., 2005). In the Supplement, we further discuss these two main features in the context of fitting the rule-based CVM1 (Magistrale et al., 1996, 2000) rule-based model to the profile A–A'; by perturbing the locations of the loosely constrained geological contacts that define the CVM1, we can analyse the outcomes of our fully 3D inversion in terms of geological structure, and find that the steep basin sidewall is consistent with recently ($\leq$4 Ma) active deformation, as suggested by our discussion here.

5 Conclusion

We use Love waves generated by the Mw 6.4 and Mw 7.1 Ridgecrest, CA earthquakes to obtain Love-wave phase velocities and relative amplitudes between 4–10 s period using the Caltech-LAUSD Community Seismic Network, which offers unprecedented high-density coverage of the northeast LA basin. We use the level-set method of Muir & Tsai (2020) to develop a parsimonious velocity inversion that updates the SCEC CVM-S background model only where empirical estimates of data uncertainty indicate addi-

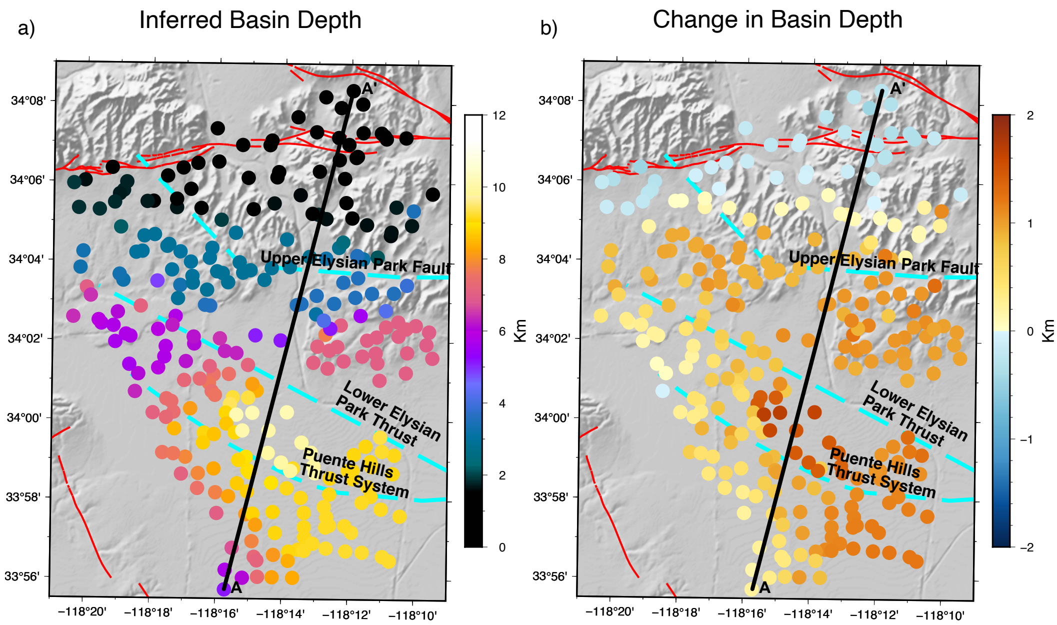

Figure 11. a) Mean depth of the inferred basin interface from the final ensemble. b) The inferred change in the depth of the Los Angeles Basin relative to CVM-S, showing deepening of the basin especially south of the Upper Elysian Park fault (top thick dashed cyan line), and shallowing of the model in the hilly terrain to the North of the CSN. In both panels, major late Quaternary faults (<130 Kyr) are shown in red, other Quaternary faults are shown in thick dashed cyan. The transect A-A' is shown in black.

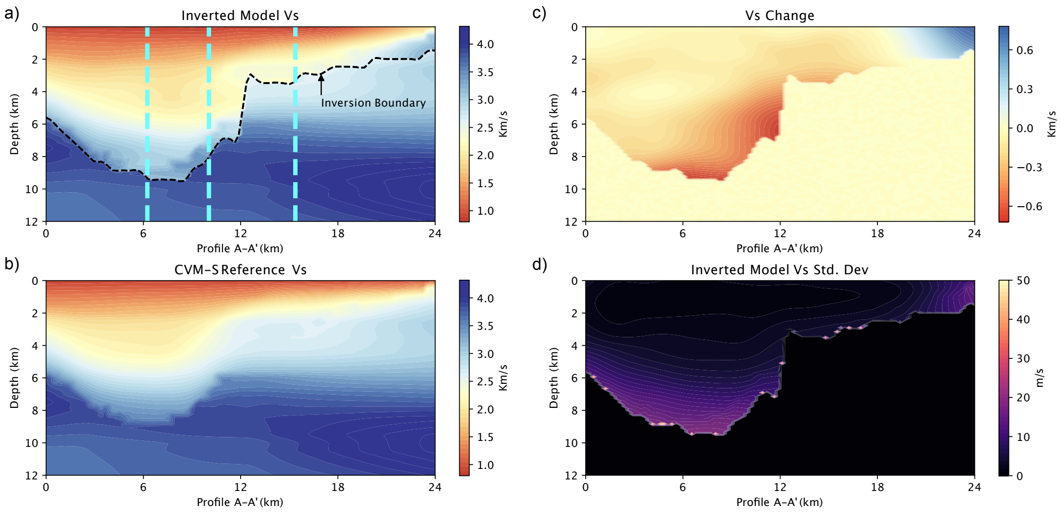

Figure 12. a) Mean of the final ensemble V_S model, b) CVM-S reference model V_S, c) difference between final model and reference model, d) standard deviation of the final ensemble V_S model.

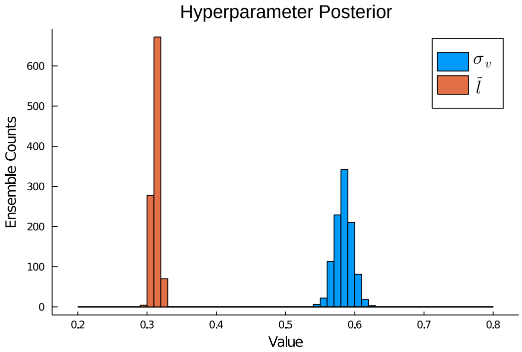

Figure 13. Approximate posterior distribution from the final ensemble for the hyperparameters $\tilde{l}$ and σ_v.

tional complexity is warranted. By employing fully 3D surface-wave inversion, we avoid internal artifacts in the model and make best use of a relatively small dataset. In doing so, we find that the northeast wall of the LA basin is substantially steeper than that of the CVM-S model, allowing for high amplifications of surface waves in the 4–6 s period band travelling within the basin. The constraints provided by this model cover some of the parts of LA with the highest density of population, infrastructure and commercial development, and highlight the continued importance of seismic velocity model evolution in providing the most accurate possible estimates of potential strong ground motions in this important city.

Acknowledgments

This study was supported by the United States National Science Foundation awards EAR-1520081, EAR-2105358 and EAR-2011079, and the southern California Earthquake Center award 20024. JBM acknowledges the support of the General Sir John Monash Foundation and the Origin Energy Foundation for support during his graduate studies. The CSN data used in this paper are freely available from `http://csn.caltech.edu/data`.

Appendix A Hierarchical Ensemble Kalman Sampler

The Ensemble Kalman Inversion (EKI) scheme was introduced by Iglesias et al. (2013) by deriving an state-variable augmented Ensemble Kalman Filter (Evensen, 1994, 2003) with dynamics that approximated the Levenberg-Marquardt method. EKI acts as an efficient black-box optimizer for large scale PDE constrained problems for which it is intractable or infeasible to obtain gradients, and has been used successfully in practical geophysical applications (e.g. Muir & Tsai (2020); Tso et al. (2021)). Subsequent to its initial formulation, much analysis on the EKI scheme has been performed by studying it as a continuous time gradient flow (Kovachki & Stuart, 2018), rather than in its original formulation as a discrete time dynamical system. This has lead to the development of the Ensemble Kalman Sampler (EKS, Garbuno-Inigo et al. (2020)), an algorithm for approximate sampling of the posterior distributions of large-scale Bayesian PDE constrained inverse problems. We utilize a hierarchical variant of the EKS scheme in this study to sample the posterior distribution of our local model update — we will briefly reintroduce the EKS scheme as described in Garbuno-Inigo et al. (2020) and then outline our variant hierarchical formulation. In general, the objective of these schemes is to approximate a posterior distribution whose negative log-posterior is of the form

$$\Phi(u, d) = ||d - G(u)||_\Gamma + R(u), \tag{A1}$$

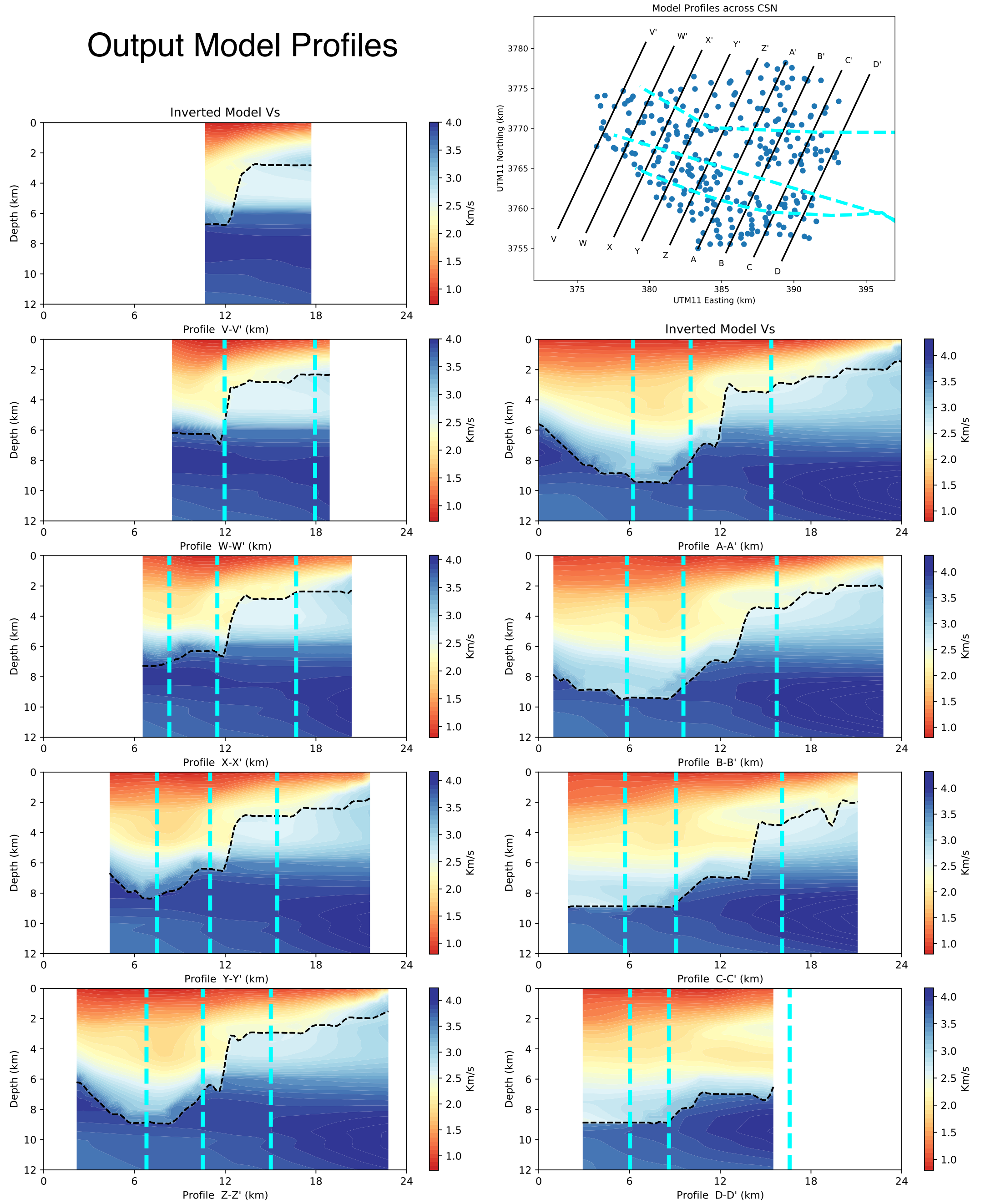

Figure 14. Profiles of the mean output V_s across the Los Angeles Basin, with inferred Quaternary faults in dashed cyan and the inferred edge of the inversion shown in dashed black.

where Γ is the data noise covariance matrix, and where the regularization term $R(u)$ introduces prior information; for instance, a typical choice would be a Tikhonov style regularization term $R(u) = ||u||_{C_0}$ for some prior covariance matrix C_0. The norms here are defined by $||u||_A = \langle u, u\rangle_A = u^T A^{-1} u$.

The EKS scheme is an ensemble-based approximation of a preconditioned overdamped Langevin equation, which is a stochastic differential equation (SDE) of the form

$$\dot{u} = -C(u)\nabla_u \Phi(u) + \sqrt{2C(u)}\dot{W} \tag{A2}$$

with $C(u)$ a preconditioning operator that depends on u and $\dot{W}$ a Brownian motion term. It can be shown that the long-term behavior of this SDE gives rise to a trajectory that has a distribution given by $p(u|d) \propto \exp(-\Phi(u,d))$ — i.e. the desired target posterior (Gelman et al., 1997). In the EKS scheme, an ensemble of particles $U = \{u^{(j)}\}_{j=1}^{J}$ are used to approximate the gradient of the likelihood, and $C(u)$ to be is chosen to be the empirical covariance $C(U) = \frac{1}{J}\sum_{j=1}^{J}(u^{(j)}-\bar{u})(u^{(j)}-\bar{u})^T$, where overbars denote means across the particle ensemble. Preconditioning by the empirical covariance acts to approximate the local curvature of the posterior by the ensemble, giving accelerated convergence compared to the unconditioned equation in a similar manner to the difference between Newton's method and gradient descent. The dynamics of this system of particles are given by the following SDE (without the gradient approximation and for Tikhonov-style Gaussian priors)

$$\dot{u}^{(j)} = \frac{1}{J}\sum_{k=1}^{J}\langle(\nabla_u G(u^{(j)})(u^{(k)}-\bar{u}), G(u^{(j)}-d)\rangle_\Gamma u^{(k)} - C(U)C_0^{-1}u^{(j)} + \sqrt{2C(U)}\dot{W}^{(j)}. \tag{A3}$$

Making the ensemble approximation for the gradient of the forward operator G allows us to rewrite this in a form without an explicit derivative:

$$\dot{u}^{(j)} = \frac{1}{J}\sum_{k=1}^{J}\langle(G(u^{(k)}) - \bar{G}, G(u^{(j)}) - d)\rangle_\Gamma u^{(k)} - C(U)C_0^{-1}u^{(j)} + \sqrt{2C(U)}\dot{W}^{(j)}, \tag{A4}$$

which is the equation solved by the EKS as described by Garbuno-Inigo et al. (2020). We will define $D(U) = \frac{1}{J}\sum_{k=1}^{J}\langle(G(u^{(k)})-\bar{G}, G(u^{(j)})-d)\rangle_\Gamma$ for future convenience, so that the dynamics for the whole ensemble are given by

$$\dot{U} = UD(U)^T - C(U)C_0^{-1}U + \sqrt{2C(U)}\dot{W}. \tag{A5}$$

We note that at the equilibrium of the ensemble, these dynamics suggest a balance between a Newton-style update of the ensemble (using an empirical covariance matrix to approximate the inverse Hessian) converging to the maximum *a posteriori* point, and the generation of correlated noise scaled to the original ensemble. The final state therefore results in a local Guassian approximation of the posterior.

Often, in geophysical problems, the scale of appropriate regularization (i.e. the choice of operator C_0 for Tikhonov regularized problems) is unknown. As such, much recent effort has been devoted to the development of hierarchical methods for solving inverse problems, in which the prior itself is to some degree unknown and is controlled by some number of hyperparameters (see e.g. Malinverno & Briggs (2004)). Additionally, for large-scale problems with Gaussian priors, it may be beneficial for efficient sampling to perform a coordinate transform into diagonalized non-centered coordinates, which remove the correlations in the prior between hyperparameters and the main parameters used in the inverse problem. This class of parametrizations are known as whitened, non-centered hierarchical parametrizations (Chada, 2018; Chada et al., 2018; Chen et al., 2019). The set of parameters is given by a collection of "regular" parameters ξ and hyperparameters θ. For zero-mean Gaussian priors, the coordinate transform is given by $u = L(\theta)\xi$ for a Cholesky factor $C_0(\theta) = L(\theta)L(\theta)^T$. With this transform, the prior for the parameters ξ is simply a Gaussian with identity covariance matrix. For reasons of computational efficiency, if the prior covariance C_0 is associated with spatial structure (say if the values of u represent material quantities at particular points in space) an approximate transform based on the solution to a stochastic partial differential equation (SPDE) is used (Lindgren et al., 2011), with the choice of SPDE determined by the particular form of the Gaussian prior to be approximated. For certain choices of prior covariance, and by defining known boundary conditions on a rectangular volume encompassing the model parameters, there are known analytic solutions for the appropriate eigenfunctions $\phi_i(\theta)$ and eigenvalues $\nu_i(\theta)$ with which to solve the SPDE such that truncation of the series of eigenfunctions has the smallest total mean squared error; these eigenfunction-eigenvalue pairs form the Karhunen-Loève (KL) expansion (Dashti & Stuart, 2013). Using the KL expansion, $L(\theta)\xi \sim \sqrt{\nu_i(\theta)}\phi_i(\theta)\xi_i$. By using these known analytic eigenfunctions and appropriately truncating the KL expansion to a reasonable number of eigenfunctions can drastically increase the speed of performing the coordinate transform; for the commonly used Whittle-Matérn family of covariance functions in a rectangular domain, the transform (assuming Neumann boundary conditions) can be calculated using the inverse discrete cosine transform for even greater efficiency.

The hyperparameters θ may have arbitrary priors ρ, which are typically non-Gaussian but do not depend on ξ; consequently the dynamics of the system follow (for ensembles $\Xi = \{\xi^{(j)}\}_{j=1}^{J}$, $\Theta = \{\theta^{(j)}\}_{j=1}^{J}$)

$$\dot{\Xi} = \Xi D(L(\Theta)\Xi)^T - C(\Xi)\Xi + \sqrt{2C(\Xi)}\dot{W} \tag{A6}$$

$$\dot{\Theta} = \Theta D(L(\Theta)\Xi)^T + C(\Theta)\nabla_\theta \log(\rho(\Theta)) + \sqrt{2C(\Theta)}\dot{W}. \tag{A7}$$

These dynamics derive from the original EKS by considering an augmented state vector $u = [\xi, \theta]^T$ and allowing arbitrary priors. We have furthermore neglected the cross-covariance terms $\mathrm{Cov}(\Xi, \Theta)$ and assumed a block-diagonal form for the preconditioning matrix, allowing us to decouple the dynamics as above. In order to solve these equations, we use the same split-step implicit scheme as Garbuno-Inigo et al. (2020), which is given by

$$\Xi_{k+1}^* = \Xi_k - \Delta t_k \Xi_k D(L(\Theta_k)\Xi_k)^T - \Delta t_k C(\Xi_k)\Xi_{k+1}^* \tag{A8}$$

$$\Theta_{k+1}^* = \Theta_k - \Delta t_k \Theta_k D(L(\Theta_k)\Xi_k)^T + \Delta t_k C(\Theta_k)\nabla_\theta \log(\rho(\Theta_{k+1}^*)) \tag{A9}$$

$$\Xi_{k+1} = \Xi_{k+1}^* + \sqrt{2\Delta t_k C(\Xi_k)} W(\Xi)_k \tag{A10}$$

$$\Theta_{k+1} = \Theta_{k+1}^* + \sqrt{2\Delta t_k C(\Theta_k)} W(\Theta)_k, \tag{A11}$$

where $W(\Xi)_k$ and $W(\Theta)_k$ are matrices of standard random normals of the same shape as Ξ and Θ respectively. The timestep Δt_k is calculated adaptively following Kovachki & Stuart (2018). Given a reference timestep Δt_0 we have $\Delta t_k = \Delta t_0/(||D(L(\Theta_k)\Xi_k)||+\delta)$ where the norm on D is the Frobenius norm and δ is an arbitrary positive constant. Unlike in Garbuno-Inigo et al. (2020), the inclusion of arbitrary non-Gaussian priors for the hyperparameters θ mean that the implicit update is no longer linear, but as the dimension of θ is usually small, the cost of performing this update using an iterative non-linear solver is normally not overly burdensome - in practice we use forward-mode automatic differentiation for arbitrary priors ρ and the L-BFGS method (Liu & Nocedal, 1989) for solving the implicit update for Θ.

References

Bowden, D. C., & Tsai, V. C. (2017, January). Earthquake ground motion amplification for surface waves: Ground Motions for Surface Waves. *Geophysical Research Letters*, *44*(1), 121–127. doi: 10.1002/2016GL071885

Bowden, D. C., Tsai, V. C., & Lin, F. C. (2015, March). Site amplification, attenuation, and scattering from noise correlation amplitudes across a dense array in Long Beach, CA. *Geophysical Research Letters*, *42*(5), 1360–1367. doi: 10.1002/2014GL062662

Bowden, D. C., Tsai, V. C., & Lin, F.-C. (2017, December). Amplification and Attenuation Across USArray Using Ambient Noise Wavefront Tracking: USArray Noise Amplitudes. *Journal of Geophysical Research: Solid Earth*, *122*(12), 10,086–10,101. doi: 10.1002/2017JB014804

Brissaud, Q., Bowden, D. C., & Tsai, V. C. (2020, June). Extension of the Basin Rayleigh-Wave Amplification Theory to Include Basin-Edge Effects. *Bulletin of the Seismological Society of America*, *110*(3), 1305–1322. doi: 10.1785/0120190161

Brocher, T. A. (2005, December). Empirical relations between elastic wavespeeds and density in the earth's crust. *Bulletin of the Seismological Society of America*, *95*(6), 2081–2092. doi: 10.1785/0120050077

Castellanos, J. C., Clayton, R. W., & Juarez, A. (2020, May). Using a Time-Based Subarray Method to Extract and Invert Noise-Derived Body Waves at Long Beach, California. *Journal of Geophysical Research: Solid Earth*, *125*(5). doi: 10.1029/2019JB018855

Chada, N. K. (2018, January). Analysis of Hierarchical Ensemble Kalman Inversion. *arXiv:1801.00847 [math]*.

Chada, N. K., Iglesias, M. A., Roininen, L., & Stuart, A. M. (2018, May). Parameterizations for ensemble Kalman inversion. *Inverse Problems*, *34*(5), 055009. doi: 10.1088/1361-6420/aab6d9

Chen, V., Dunlop, M. M., Papaspiliopoulos, O., & Stuart, A. M. (2019, March). Dimension-Robust MCMC in Bayesian Inverse Problems. *arXiv:1803.03344 [stat]*.

Clayton, R. W., Heaton, T., Chandy, M., Krause, A., Kohler, M., Bunn, J., … Aivazis, M. (2012, January). Community Seismic Network. *Annals of Geophysics*, *54*(6), 738–747. doi: 10.4401/ag-5269

Clayton, R. W., Kohler, M., Guy, R., Bunn, J., Heaton, T., & Chandy, M. (2020, March). CSN-LAUSD Network: A Dense Accelerometer Network in Los Angeles Schools. *Seismological Research Letters*, *91*(2A), 622–630. doi: 10.1785/0220190200

Dashti, M., & Stuart, A. M. (2013, February). The Bayesian Approach To Inverse Problems. *arXiv:1302.6989 [math]*.

Datta, A. (2018, March). SWRT: A package for semi-analytical solutions of surface wave propagation, including mode conversion, across transversely aligned vertical discontinuities. *Geoscientific Instrumentation, Methods and Data Systems*, *7*(1), 101–112. doi: 10.5194/gi-7-101-2018

Evensen, G. (1994). Sequential data assimilation with a nonlinear quasi-geostrophic model using Monte Carlo methods to forecast error statistics. *Journal of Geophysical Research*, *99*(C5), 10143. doi: 10.1029/94JC00572

Evensen, G. (2003, November). The Ensemble Kalman Filter: Theoretical formulation and practical implementation. *Ocean Dynamics*, *53*(4), 343–367. doi: 10.1007/s10236-003-0036-9

Faust, L. Y. (1951, April). Seismic velocity as a function of depth and geologic time. *GEOPHYSICS*, *16*(2), 192–206. doi: 10.1190/1.1437658

Filippitzis, F., Kohler, M. D., Heaton, T. H., Graves, R. W., Clayton, R. W., Guy, R. G., … Chandy, K. M. (2021, April). Ground motions in urban Los Angeles from the 2019 Ridgecrest earthquake sequence. *Earthquake Spectra*, 875529302110039. doi: 10.1177/87552930211003916

Garbuno-Inigo, A., Hoffmann, F., Li, W., & Stuart, A. M. (2020, January). Interacting Langevin Diffusions: Gradient Structure and Ensemble Kalman Sampler. *SIAM Journal on Applied Dynamical Systems*, *19*(1), 412–441. doi: 10.1137/19M1251655

Gelman, A., Gilks, W. R., & Roberts, G. O. (1997, February). Weak convergence and optimal scaling of random walk Metropolis algorithms. *The Annals of Applied*

Probability, *7*(1). doi: 10.1214/aoap/1034625254
Graves, R. W., & Pitarka, A. (2010, October). Broadband Ground-Motion Simulation Using a Hybrid Approach. *Bulletin of the Seismological Society of America*, *100*(5A), 2095–2123. doi: 10.1785/0120100057
Haney, M. M., & Tsai, V. C. (2015, November). Nonperturbational surface-wave inversion: A Dix-type relation for surface waves. *GEOPHYSICS*, *80*(6), EN167-EN177. doi: 10.1190/geo2014-0612.1
Haney, M. M., & Tsai, V. C. (2017, May). Perturbational and nonperturbational inversion of Rayleigh-wave velocities. *GEOPHYSICS*, *82*(3), F15-F28. doi: 10.1190/geo2016-0397.1
Haney, M. M., & Tsai, V. C. (2020, January). Perturbational and nonperturbational inversion of Love-wave velocities. *GEOPHYSICS*, *85*(1), F19-F26. doi: 10.1190/geo2018-0882.1
Iglesias, M. A., Law, K. J. H., & Stuart, A. M. (2013, April). Ensemble Kalman methods for inverse problems. *Inverse Problems*, *29*(4), 045001. doi: 10.1088/0266-5611/29/4/045001
Ingersoll, R. V., & Rumelhart, P. E. (1999). Three-stage evolution of the Los Angeles basin, southern California. *Geology*, *27*(7), 593–596.
Jia, Z., & Clayton, R. W. (2021, May). Determination of Near Surface Shear-Wave Velocities in the Central Los Angeles Basin With Dense Arrays. *Journal of Geophysical Research: Solid Earth*, *126*(5). doi: 10.1029/2020JB021369
Kohler, M. D., Filippitzis, F., Heaton, T., Clayton, R. W., Guy, R., Bunn, J., & Chandy, K. M. (2020, November). 2019 Ridgecrest Earthquake Reveals Areas of Los Angeles That Amplify Shaking of High-Rises. *Seismological Research Letters*, *91*(6), 3370–3380. doi: 10.1785/0220200170
Kovachki, N. B., & Stuart, A. M. (2018, August). Ensemble Kalman Inversion: A Derivative-Free Technique For Machine Learning Tasks. *arXiv:1808.03620 [cs, math, stat]*.
Lai, V. H., Graves, R., Zhan, Z., Yu, C., & Helmberger, D. (2019). Analyzing Shallow Basin Effects in Los Angeles Basin using 3D Simulations and Dense Array Analysis. In *SCEC Annual Meeting* (Vol. Contribution 9804).
Lai, V. H., Graves, R. W., Yu, C., Zhan, Z., & Helmberger, D. V. (2020, October). Shallow Basin Structure and Attenuation Are Key to Predicting Long Shaking Duration in Los Angeles Basin. *Journal of Geophysical Research: Solid Earth*, *125*(10). doi: 10.1029/2020JB019663
Lee, E.-J., Chen, P., Jordan, T. H., Maechling, P. B., Denolle, M. A. M., & Beroza, G. C. (2014). Full-3-D tomography for crustal structure in Southern California based on the scattering-integral and the adjoint-wavefield methods. *Journal of Geophysical Research: Solid Earth*, *119*(8), 6421–6451. doi: 10.1002/2014JB011346
Lin, F.-C., Li, D., Clayton, R. W., & Hollis, D. (2013, July). High-resolution 3D shallow crustal structure in Long Beach, California: Application of ambient noise tomography on a dense seismic array. *GEOPHYSICS*, *78*(4), Q45-Q56. doi: 10.1190/geo2012-0453.1
Lin, F.-C., & Ritzwoller, M. H. (2011, September). Helmholtz surface wave tomography for isotropic and azimuthally anisotropic structure: Helmholtz surface wave tomography. *Geophysical Journal International*, *186*(3), 1104–1120. doi: 10.1111/j.1365-246X.2011.05070.x
Lin, F.-C., Ritzwoller, M. H., & Snieder, R. (2009, June). Eikonal tomography: Surface wave tomography by phase front tracking across a regional broad-band seismic array. *Geophysical Journal International*, *177*(3), 1091–1110. doi: 10.1111/j.1365-246X.2009.04105.x
Lin, F. C., Tsai, V. C., & Schmandt, B. (2014, August). 3-D crustal structure of the western United States: Application of Rayleigh-wave ellipticity extracted from

noise cross-correlations. *Geophysical Journal International*, *198*(2), 656–670. doi: 10.1093/gji/ggu160

Lindgren, F., Rue, H., & Lindström, J. (2011, September). An explicit link between Gaussian fields and Gaussian Markov random fields: The stochastic partial differential equation approach: Link between Gaussian Fields and Gaussian Markov Random Fields. *Journal of the Royal Statistical Society: Series B (Statistical Methodology)*, *73*(4), 423–498. doi: 10.1111/j.1467-9868.2011.00777.x

Liu, D. C., & Nocedal, J. (1989, August). On the limited memory BFGS method for large scale optimization. *Mathematical Programming*, *45*(1-3), 503–528. doi: 10.1007/BF01589116

Lysmer, J. (1970). Lumped Mass Method for Rayleigh Waves. *Bulletin of the Seismological Society of America*, *60*(1), 89-&.

Magistrale, H., Day, Steven, Clayton, Robert W., & Graves, Robert. (2000, December). The SCEC Southern California Reference Three-Dimensional Seismic Velocity Model Version 2. *Bulletin of the Seismological Society of America*, *90*(6B), S65-S76. doi: 10.1785/0120000510

Magistrale, H., McLaughlin, K., & Day, S. (1996, August). A geology-based 3D velocity model of the Los Angeles basin sediments. *Bulletin of the Seismological Society of America*, *86*(4), 1161–1166.

Malinverno, A., & Briggs, V. A. (2004, July). Expanded uncertainty quantification in inverse problems: Hierarchical Bayes and empirical Bayes. *Geophysics*, *69*(4), 1005–1016. doi: 10.1190/1.1778243

Muir, J., & Tsai, V. (2020, February). Geometric and level set tomography using ensemble Kalman inversion. *Geophysical Journal International*, *220*(2), 967–980. doi: 10.1093/gji/ggz472

Pitarka, A., Graves, R. W., & Rodgers, A. J. (2019, December). Strong Ground Motion Simulation for the M7.1, 2019 Ridgecrest California Earthquake. *AGU Fall Meeting Abstracts*, *31*.

Plesch, A., Shaw, J. H., Benson, C., Bryant, W. A., Carena, S., Cooke, M., … Yeats, R. (2007, December). Community Fault Model (CFM) for Southern California. *Bulletin of the Seismological Society of America*, *97*(6), 1793–1802. doi: 10.1785/0120050211

Qiu, H., Lin, F.-C., & Ben-Zion, Y. (2019, September). Eikonal Tomography of the Southern California Plate Boundary Region. *Journal of Geophysical Research: Solid Earth*, *124*(9), 9755–9779. doi: 10.1029/2019JB017806

Rasmussen, C. E., & Williams, C. K. I. (2006). *Gaussian processes for machine learning.* Cambridge, Mass: MIT Press.

SciPy 1.0 Contributors, Virtanen, P., Gommers, R., Oliphant, T. E., Haberland, M., Reddy, T., … van Mulbregt, P. (2020, March). SciPy 1.0: Fundamental algorithms for scientific computing in Python. *Nature Methods*, *17*(3), 261–272. doi: 10.1038/s41592-019-0686-2

Shaw, J. H., Plesch, A., Tape, C., Suess, M. P., Jordan, T. H., Ely, G., … Munster, J. (2015, April). Unified Structural Representation of the southern California crust and upper mantle. *Earth and Planetary Science Letters*, *415*, 1–15. doi: 10.1016/j.epsl.2015.01.016

Süss, M. P., & Shaw, J. H. (2003). Pwave seismic velocity structure derived from sonic logs and industry reflection data in the Los Angeles basin, California. *Journal of Geophysical Research: Solid Earth*, *108*(B3). doi: 10.1029/2001jb001628

Taborda, R., Azizzadeh-Roodpish, S., Khoshnevis, N., & Cheng, K. (2016, June). Evaluation of the southern California seismic velocity models through simulation of recorded events. *Geophysical Journal International*, *205*(3), 1342–1364. doi: 10.1093/gji/ggw085

Tape, C., Liu, Q., Maggi, A., & Tromp, J. (2009, August). Adjoint Tomography of the Southern California Crust. *Science*, *325*(5943), 988–992. doi: 10.1126/science

.1175298

Tsai, V. C., & Atiganyanun, S. (2014, October). Green's Functions for Surface Waves in a Generic Velocity Structure. *Bulletin of the Seismological Society of America*, *104*(5), 2573–2578. doi: 10.1785/0120140121

Tso, C.-H. M., Iglesias, M., Wilkinson, P., Kuras, O., Chambers, J., & Binley, A. (2021, February). Efficient multiscale imaging of subsurface resistivity with uncertainty quantification using ensemble Kalman inversion. *Geophysical Journal International*, *225*(2), 887–905. doi: 10.1093/gji/ggab013

USGS. (2020). *U.S. Geological Survey and California Geological Survey, Quaternary fault and fold database for the United States, https://www.usgs.gov/natural-hazards/earthquake-hazards/faults, Accessed April 12, 2021.* USGS.

Wright, T. L. (1991). Structural Geology and Tectonic Evolution of the Los Angeles Basin, California. In *Active Margin Basins* (pp. 35–134). American Association of Petroleum Geologists: AAPG Special Volumes.

Yerkes, R. F., Campbell, R. H., Alvarez, R. M., & Bovard, K. R. (2005). Preliminary geologic map of the Los Angeles $30' \times 60'$ Quadrangle, southern California. *US Geological Survey Open File Report*, *1019*, 1559–1573.